Waste Management Bulletin 3 (2025) 100260

Contents lists available at ScienceDirect

Waste Management Bulletin

journal homepage: www.elsevier.com/locate/wmb

Inventory of the mining wastes located at the Iberian Pyrite Belt (IPB)

Juan Antonio Ramírez-Pérez [a,*], Felipe Jesús González Barrionuevo [b], Manuel Jesús Gázquez-González [c], Reinaldo Sáez Ramos [b], Juan Pedro Bolívar [a]

[a] Department of Integrated Sciences, Center for Natural Resources, Health and Environment (RENSMA), University of Huelva 21071, Huelva, Spain
[b] Department of Earth Sciences, University of Huelva 21071, Huelva, Spain
[c] Department of Applied physics, Marine Research Institute (INMAR), University of Cádiz, 11510 Puerto, Real, Spain

A B S T R A C T

The Iberian Pyrite Belt (IPB), located in the SW of Iberian Peninsula, hosts the largest massive sulfide deposit globally, and over two centuries of intensive mining activity have generated huge amounts of abandoned mining waste along this region. Due to the limited information on the volume of the mining tailings, the main objective of this study has been to develop a volumetric inventory of these wastes by using Unmanned Aerial Vehicles (UAVs). For this purpose, Digital Elevation Models (DEM) and Triangular Irregular Networks (TIN) were developed, finding that the estimated waste reserves were 23.3 Mt ($1.77 \bullet 10^7$ m^3) for the selected mining areas. The concentrations of both major and trace elements, and natural radionuclides were determined. Total reserves of Fe (2.12 Mt in Almagrera, Sotiel Coronada), and other metals/metalloids were calculated; highlighting 0.05 Mt for Zn in Riotinto, 0.06 Mt for Pb in Sotiel Coronada and 989 t for Rare Earth Elements in total. Nevertheless, natural radionuclide levels are similar to those found for unperturbed soils (25 Bq kg^{-1} of ^{238}U, 21 Bq kg^{-1} of ^{232}Th, and 224 Bq kg^{-1} for ^{40}K). As potential applications for these mining stockpiles, techniques of Fe, Zn, Pb and REE recovery and uses as building materials are proposed for their valorization and to promote the circular economy.

Introduction

The Iberian Pyrite Belt (IPB), at the southwest Iberian Peninsula, extends through parts of Spain and Portugal. This region is notable for containing the planet's most extensive concentration of massive sulfide ore deposits (Inverno et al., 2015). Initial reserves of pyrite about 1700 Mt have been assessed (Yesares et al., 2023). Mining and metallurgical activities have taken place in the area since around 4500 BCE, continuing into modern times (Grande et al., 2010). The intensive extraction and processing activities, especially prominent during the late 1800 s and early 1900 s, have generated widespread accumulation of mining residues at multiple sites, particularly along the Odiel and Tinto River basins. These locations are commonly known as "legacy sites".

Many of these mining residues are characterized by high concentrations of toxic metals and metalloids, such as arsenic and various heavy metals (Pb, Cu, Zn, etc.). Additionally, metallic mining is classified as Naturally Occurring Radioactive Material (NORM) activities, in accordance with applicable Spanish legislation (Santos et al., 2022). Consequently, these legacy sites may pose considerable environmental, safety, and public health risks, especially given their frequent proximity to populated areas and ecologically vulnerable aquatic systems, as observed in the case under study (Álvarez-Valero et al., 2009; Karachaliou et al., 2016).

There is currently significant interest in assessing and cataloguing the various types of abandoned mining wastes present in this region, with the objective to support future remediation efforts and, where feasible, to estimate their volumes to evaluate potential valorization pathways. This study specifically addresses these aspects. It should be mentioned that, despite the large number of studies, analyses and inventories of mining wastes in this area (Grande et al., 2014; Pinedo Vara, 1963), there is no inventory of waste volumes and masses, so this would be the first to provide such data. In parallel, several international studies have addressed similar issues related to the environmental evaluation of mining activities and residues (Kruzhilko et al., 2024; Gumbo & Kapenge, 2025), including the use of life cycle assessment (LCA) approaches to support sustainable management and valorization strategies (Abah et al., 2025).

To accurately assess the volumes of mining waste stockpiles, several researchers have suggested employing Unmanned Aerial Vehicles (UAVs) for tasks such as topographic mapping and environmental monitoring (Ajayi et al., 2020). UAV-acquired imagery provides high spatial resolution and offers a faster and more flexible alternative to traditional ground surveys, while also being more cost-effective (Zietara, 2017). Additionally, UAVs make it possible to generate a Digital Elevation Model (DEM), a three-dimensional representation of

* Corresponding author.
E-mail address: juan.ramirez@dci.uhu.es (J.A. Ramírez-Pérez).

https://doi.org/10.1016/j.wmb.2025.100260

Available online 23 October 2025

terrain elevation based on pixel values, which allows for more precise calculations of waste volumes (Abdulrahman et al., 2020).

Given the potential environmental and public health risks associated with mining wastes deposited historically in uncontrolled sites, the central objective of this study was to conduct a comprehensive inventory of the major mining stockpiles located in the IPB, including estimates of their volumes and masses. Additionally, a detailed characterization of these materials was carried out to quantify the content of elements with high commercial value, with the aim of identifying potential pathways for their future valorization.

Materials and methods

Study area, sampling and sample pre-treatment

Based on the types of mining waste, the historical production volumes, and the significance of each site, mining stockpiles from 12 mines within the IPB were selected for this study: Tharsis (TH), Lagunazo (LA), Cueva de la Mora (CM), San Telmo (ST), Zarza-Perrunal (ZP), Riotinto (RT), Almagrera's ponds in Sotiel Coronada (SC), Cabezas del Pasto (CP), Nuestra Señora del Carmen (CA), Saos Domingos (SD), Herrerías (HE) and Cobre las Cruces (CC) (Fig. 1).

At each mining site, all known stockpiles were included in the survey. Field sampling was carried out in March 2025. To reduce the effects of surface weathering, the top 5 cm of material was removed prior to sampling. Approximately 1 kg of material was collected at each sampling location using a shovel and subsequently stored for pre-treatment procedures, including drying and grinding. This selected sample mass was chosen to ensure enough material for multi-elemental and radiological analyses while minimizing sample handling and transport constraints. Additionally, to determine the bulk density of the residues, their weights were measured in 38 × 65 mm plastic containers after drying and grinding.

The number of samples collected at each site mainly depended on the accessibility of the different mining stockpiles. Although all stockpiles were analyzed through UAV surveys, in some cases direct access on foot was not possible due to safety constraints or unstable slopes. Therefore, sampling was carried out in all accessible stockpiles, aiming to cover as many as possible. To ensure the reliability and representativeness of the analytical results, several subsamples were collected from different points within each accessible mound and subsequently homogenized to form a composite sample representative of the overall material.

The mining wastes considered in this study included several distinct materials. Roasted pyrite refers to the reddish ash that remains after sulfur is removed from polymetallic sulfides through roasting (Alp et al., 2009). Slags are the byproducts generated when sulfide ores are smelted at around 1200 °C, followed by cooling to recover the desired metals (de Andrade Lima & Bernardez, 2011). Jarosite ponds consist of the yellow iron hydroxysulfate $KFe_3(SO_4)_2(OH)_6$, which precipitates under highly acidic conditions (pH < 3) in waters rich in Fe^{3+} and sulfate concentrations (conditions typically associated with acid mine drainage), and tends to accumulate in stagnant zones (Eftekhari et al., 2020). Leached pyrite results from treating pyrite ores with sulfuric acid to dissolve and extract valuable metals. Atmospheric pressure leach residues were also examined, sourced from the hydrometallurgical processing at the active Cobre Las Cruces mine. Finally, flotation tailings were included, which are produced during the separation of valuable minerals by air-induced froth flotation (Mu et al., 2016).

UAV data acquisition, processing and mapping

To obtain the spatial information for estimating the volume of the stockpiles, a UAV (DJI Mavic 3 M) was used to survey the stockpiles. Equipped with 20 MP RGB camera and four 5 MP multispectral cameras, net weight with propellers is 951 g and the dimensions unfolded and without propellers are: 347.5x283x139.6 mm. Through its connection to 30 satellites by GPS it can obtain a precise location of each photo. UAV missions were also performed in March 2025 in Real Time Kinematic (RTK) mode.

The photogrammetric mission was planned using DroneDeploy, a widely used platform for aerial mapping compatible with Windows, iOS, and other operating systems. This software is also employed by DJI for the Mavic series drones. It allows the configuration of multiple flight parameters, including altitude, mapping area boundaries, camera settings, image overlap, flight speed, obstacle avoidance, and flight direction (inputs introduced for the images acquisition). Aerial images were captured by drone's camera at an altitude of 110 m and a flight speed of 15 m/s. Autonomous flight modes were implemented, following predefined paths around the mine stockpiles, with images taken approximately every 2 s, achieving an optimal image overlap of 80 % front-lap

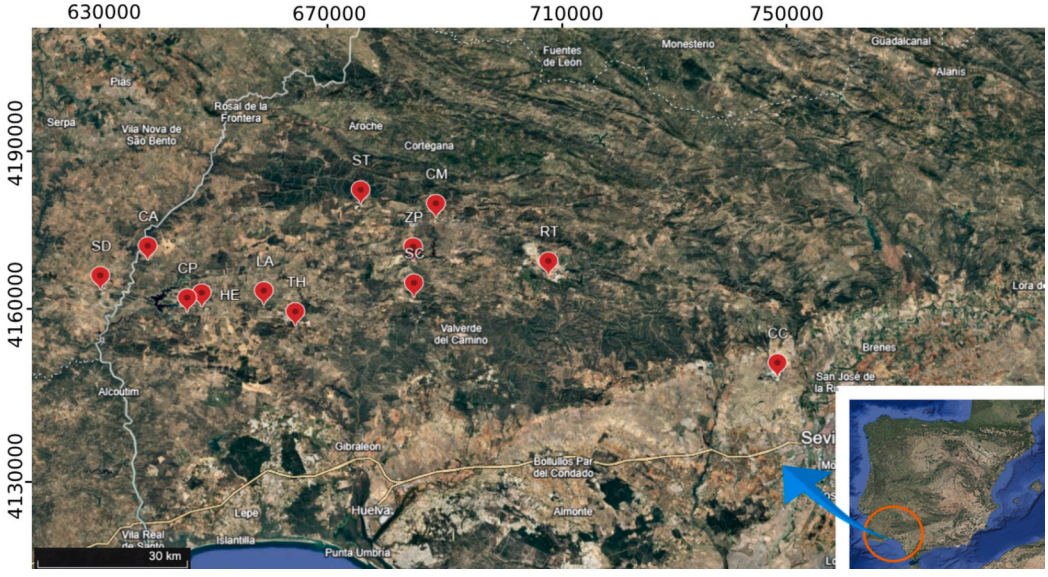

Fig. 1. Location of the studied mines. Coordinates are in ETRS89/UTM 29 N. Image from Google Earth. Codes: Tharsis (TH), Lagunazo (LA), Cueva de la Mora (CM), San Telmo (ST), Zarza-Perrunal (ZP), Riotinto (RT), Sotiel Coronada (SC), Cabezas del Pasto (CP), Nuestra Señora del Carmen (CA), Saos Domingos (SD) and Herrerías (HE), Cobre las Cruces (CC).

and 75 % side-lap.

RTK corrections were applied for positional calibration, enabling near instantaneous position fixes with centimeter-subcentimeter-level accuracy (Pirti, 2011). RTK differential correction data was obtained from *Red Andaluza de Posicionamiento* (RAP). Image processing and volume calculation were carried out using Metashape® software from Agisoft™. This photogrammetric software offered in both Standard and Pro versions. For this study, the Pro version was employed to create 3D models from two-dimensional aerial photographs and to calculate the volume of mining stockpiles.

Once all images from the flight paths are collected, the software performs an alignment process to reconstruct the scene by identifying matching features or shared elements across the photographs (Lowe, 2004), as illustrated in Fig. 2. The workflow then continues with the generation of a dense point cloud (Fig. 3), followed by the computation of a depth map for each image (Lin et al., 2018), and ultimately the creation of a Digital Elevation Model (DEM) (Ajayi et al., 2017). The geospatial reference system applied was ETRS89/UTM 29 N. To minimize distortions resulting from camera inclination or terrain relief and to improve the visualization of the stockpile, an orthomosaic is produced. This process yields a continuous image with no visible seams or borders (Szeliski, 2022).

When RTK signal was not available, the recalibration was performed using ground control points (GCP) identified in the post-processing. A minimum of 5 GCPs were selected from the digital aerial orthophotographs (0.15 m/pixel resolution) of the Spanish National Orthophoto Program (PNOA). The precision error achieved on this GCP method, 0.10 m, was comparable with the average accuracy achieved of the RTK models (0.07 m).

Finally, using the images generated by the orthomosaic, the mining waste piles can be identified, allowing for the delineation of their boundaries and the calculation of their volumes using the lower tangential plane. The entire mapping and analysis process in Agisoft is illustrated in the flowchart shown in Fig. 2.

In the case of Almagrera's ponds in Sotiel Coronada, which consist of two reinstated basins, pre-deposit mapping was performed using a 1981 topographic map at a scale of 1:25000. The contour lines were digitized, and a Triangular Irregular Network (TIN) was generated. A TIN models complex natural terrain by connecting sets of three points into non-overlapping triangles (Huang, 1989), providing a representation of the terrain before waste deposition. Later, using 2024 orthophotographs at a resolution of 0.15 m/pixel, the maximum waste fill level of the ponds was determined, allowing the calculation of the internal volume. Volumetric analysis and modeling were conducted using ArcGIS Pro software (Fig. 4).

Multi-elemental composition

Major element concentrations were determined by X-ray fluorescence (XRF) using a PANalytical ZETIUM sequential spectrometer at the Research, Technology, and Innovation Center (CITIUS), University of Seville, Spain. The spectrometer is equipped with a 4 kW rhodium-anode X-ray tube, front window, dual detectors (flow and scintillation), and five analytical crystals (PX1, PE 002, LIF 200, Ge 111, LIF 220). For analysis, 1.5 g of each dried sample was used.

Trace element analysis, particularly for Rare Earth Elements (REEs), was carried out at Activation Laboratories Ltd. (ACTLABS), an accredited facility in Ontario, Canada. Samples underwent digestion using a combination of four strong acids—hydrochloric, nitric, perchloric, and hydrofluoric—to ensure near-complete dissolution. Quantification was

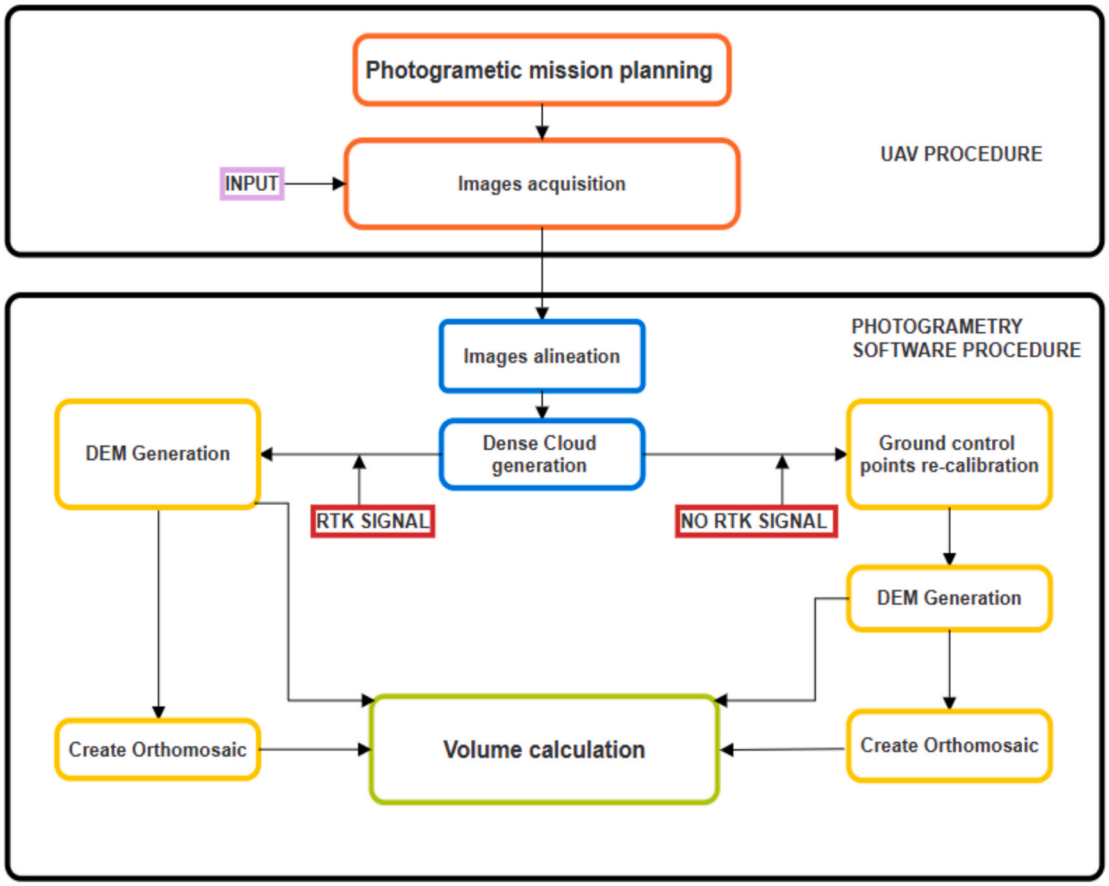

Fig. 2. Flow chart for obtaining volumes of mining stockpiles. Inputs introduced in UAV for images acquisition were altitude, mapping area boundaries, camera settings, image overlap, flight speed, obstacle avoidance, and flight direction.

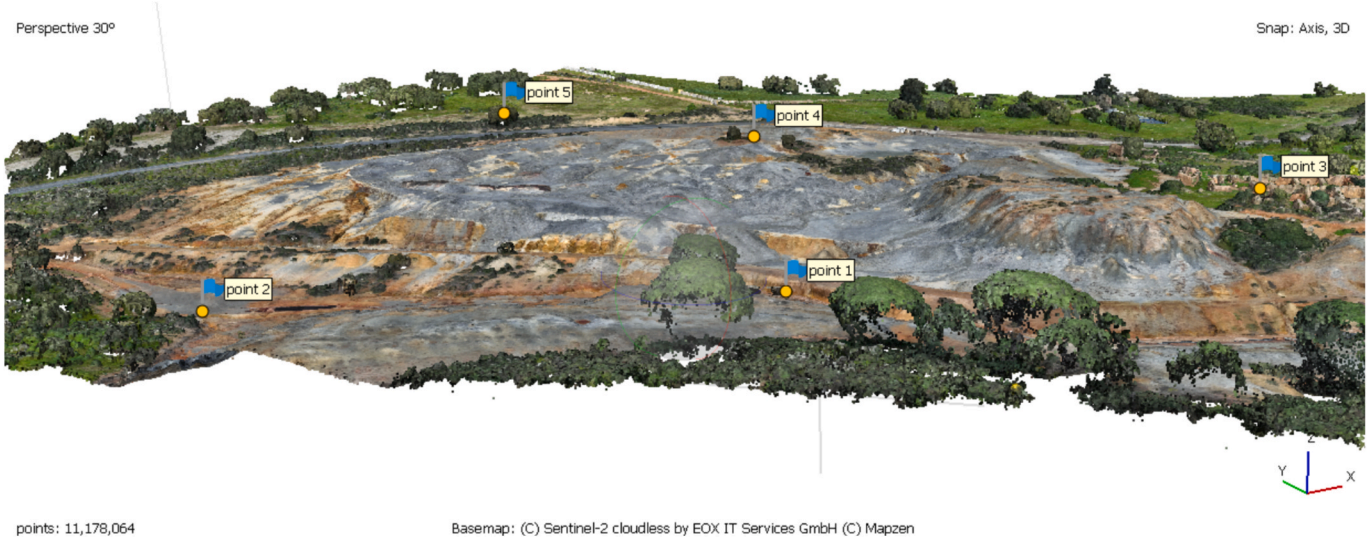

Fig. 3. Dense point cloud from Cabezas de Pasto mine. As there was no RTK signal, ground control points were used.

Fig. 4. Almagrera's ponds topography map 1:25.000 of 1981 with the perimeter superimposed in Sotiel Coronada.

performed through inductively coupled plasma optical emission spectrometry (ICP-OES), using a Varian 735ES instrument, and inductively coupled plasma mass spectrometry (ICP-MS) with an ELAN 9000 system. Rigorous quality assurance procedures were applied, including the use of blanks, duplicate samples, and a set of certified reference materials (CRM): OREAS 903, 96, 520, 683, 70b, 620, and 603c.

Radioactive characterization

Radioactive analysis was conducted through gamma spectrometry using high-purity germanium (HPGe) detectors. This method allowed for the quantification of gamma-emitting radionuclides in the samples. An extended-range HPGe detector (XtRa) with a thin beryllium window was used, enabling the measurement of low-energy gamma emissions down to approximately 20 keV. To minimize background interference, the shielding chamber was continuously purged with nitrogen gas derived from the detector's liquid nitrogen cooling system. This process displaced the ambient air and effectively eliminated radon from the interior of the shielding.

The detector had a relative efficiency of 38.4 % at 1332 keV when compared to a 3″×3″ NaI(Tl) scintillation detector. Its energy resolution, expressed as full width at half maximum (FWHM), was 1.74 keV at 1332 keV and 0.88 keV at 122 keV, with a Compton-to-peak ratio of 67.5:1 (Barba-Lobo et al., 2021). The gamma-emitting radionuclides quantified included ^{4o}K (1460.83 keV), ^{238}U via its daughter isotope ^{234}Th (63.29 keV), assumed to be in secular equilibrium with ^{238}U, and ^{232}Th, measured through ^{228}Ra, which is likewise considered in secular equilibrium with ^{228}Ac (911 keV).

Quality control

Quality control procedures were implemented for every set of ten samples and included the use of procedural blanks, duplicate analyses, and certified reference materials (IAEA-375 and IAEA-327). Additionally, intercomparison exercises were conducted to verify analytical accuracy and ensure consistency across measurements.

Results

Orthomosaics

Fig. 5 shows the different orthomosaics obtained for the different mining stockpiles analyzed following the methodology explained above. These mosaics allow a detailed visual analysis of each stockpile's shape, extent, and context within the broader landscape. The locations of control points are also shown where necessary. These orthomosaics together with the spatial boundaries were necessary for the subsequent calculation of mound volumes.

Assessment of volumes and masses of waste repositories

The estimated total volumes and areas of the different mining stockpiles, performed by the mentioned methods, are given in Table 1.

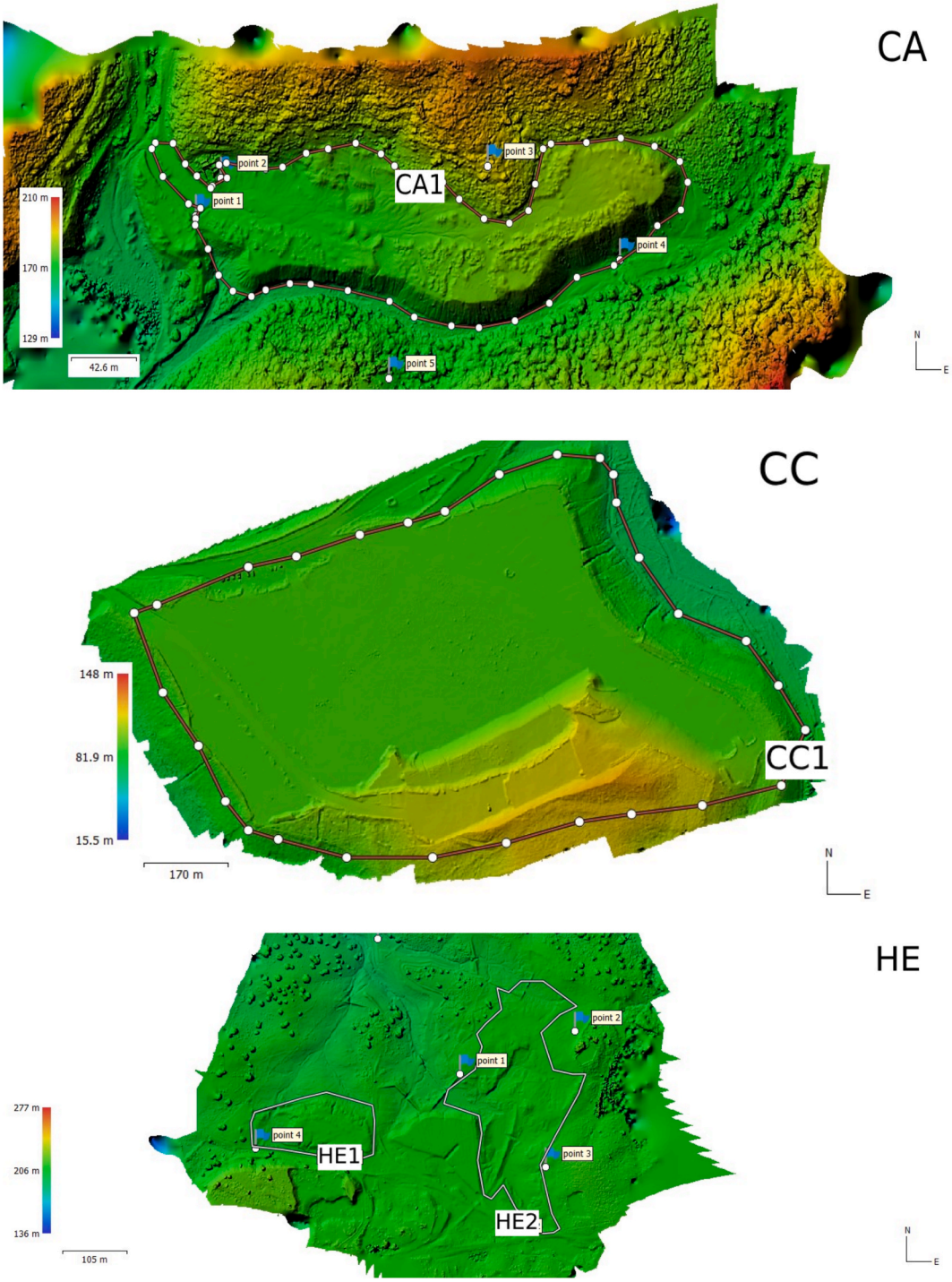

Fig. 5. Mining mounds studied from the orthomosaic generated by the DEM. The names of each mine and mounds are included. Borders of mining stockpiles are also represented by lines. Heights are included using color patterns. Due to the size, two UAV flights were conducted in Cueva de la Mora (CM) in order to cover all areas with mining stockpiles.

Since the bulk densities of wastes were previously obtained as stated in pre-treatment, total masses were calculated by multiplying the densities by their volumes. Both terms are also found in Table 1. These results are considered estimates given the uncertainty in the delineation of mine stockpile perimeters (Tucci et al., 2019). There is a high heterogeneity in the different mining stockpiles: Atmospheric pressure leaching waste (CC1), leached pyrite (TH1-4, LA1, ST1-3, ZP1, CP1, CA1, HE1-2), roasted pyrite (LA2, CM6, SC1), slags (CM1-5, RT2, SD1-2), jarosite pond (RT1) and floated pyrite (SC2).

The mining wastes deposits analyzed have a volume ranging from several orders of magnitude difference. The smallest ones are CM2, CM3 and CM4 with $6.6 \bullet 10^3$ m^3, $7.5 \bullet 10^3$ m^3 and $3.1 \bullet 10^3$ m^3, respectively. On the other hand, there are several mining stockpiles exceeding 10^6 m^3: CC1 ($3.61 \bullet 10^6$ m^3), TH4 ($2.59 \bullet 10^6$ m^3), ST1 ($2.94 \bullet 10^6$ m^3), SC1 ($2.42 \bullet 10^6$ m^3) and SC2 ($2.44 \bullet 10^6$ m^3). Similarly, there are orders of magnitude of difference in the masses of all mining mounds. Among all

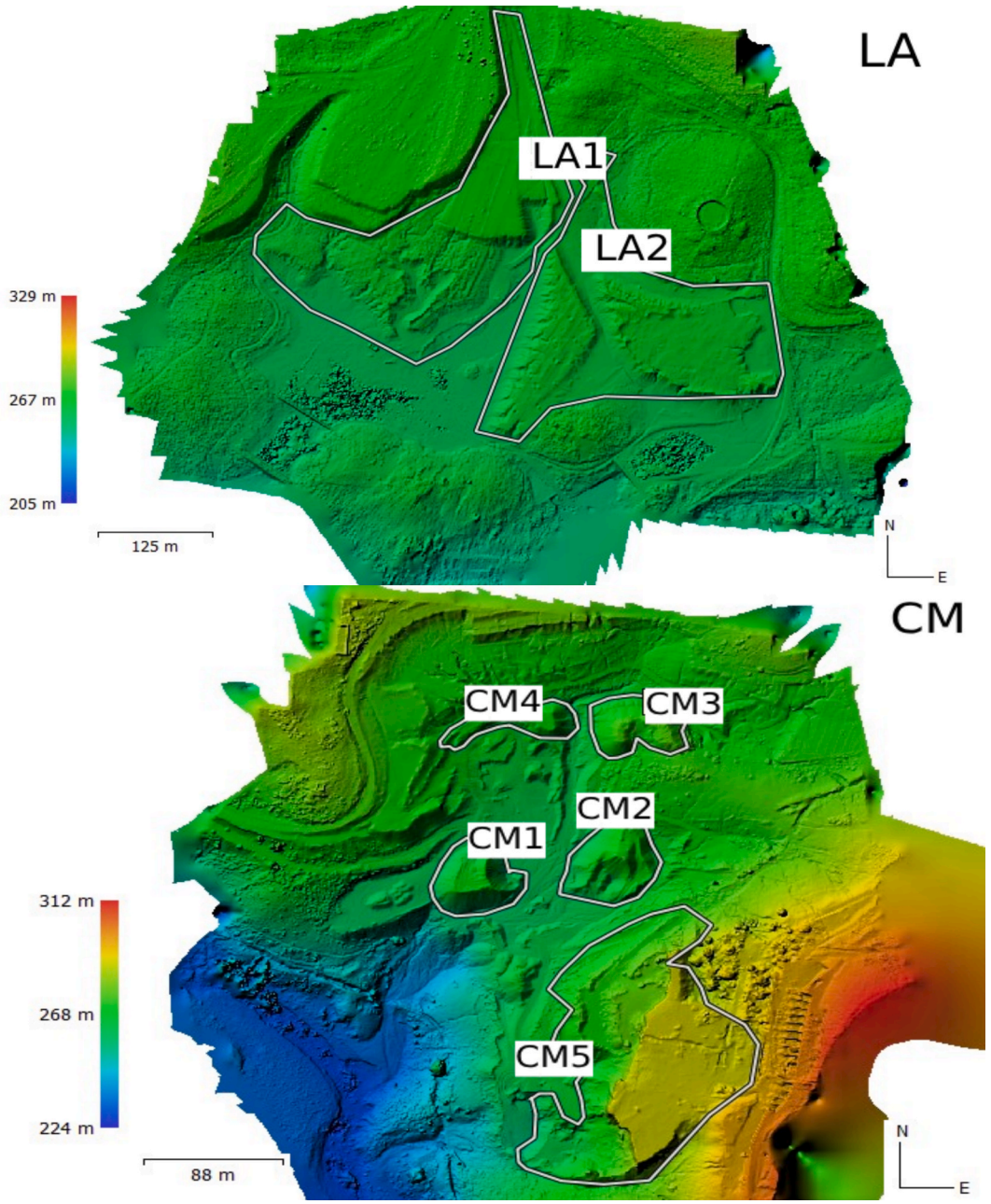

Fig. 5. (*continued*).

of them, the ones that stand out with the highest mass are CC1 (5.31 Mt), TH4 (2.54 Mt), ST1 (3.60 Mt), RT2 (1.77 Mt), SC1 (3.67 Mt) and SC2 (3.07 Mt).

It should be noted that mines with very steep or unconsolidated slopes, such as at CM, CA or TH, the mining stockpiles can be affected by erosion (Sánchez-Donoso et al., 2019). This erosion, manifested as slope slides and gullies, may be favored by high rainfalls and very dry summers, very typical in this geographical area (Martín-Velázquez et al., 2022), as well as by absence of vegetation. These considerations are significant as they may affect the volume and masses of the mining stockpiles over time.

Major elements

An analysis of the estimated reserves of the major elements, whose concentrations generally exceed 0.1 %, is shown in Table 2, including in last row the total amount for each element. These reserves were obtained by multiplying the masses estimated in Table 1 by the elemental concentrations in percentage provided by XRF. It is worth mentioning that not all mounds analyzed by UAV were sampled due to inaccessibility. The elements with the highest estimated total reserves are Fe (3.5 Mt), S (2.86 Mt) and Si (1.96 Mt), thus justifying the majority presence of pyrite and silicates in these mining environments.

In the case of iron, the estimated reserves in SC1 amount 1.84 Mt, which could represent a great opportunity for the valorization of this resource and favor the circular economy. For sulfur, the presence of 1.56 Mt of this element in SC2 has critical environmental implications, as a high probability of acid mine drainage (AMD). This favors the mobilization of toxic metals/metalloids and is a source of contamination for the ecosystem (Alam et al., 2012, Nieto et al., 2007).

On the other hand, the total estimated reserves for elements such as aluminum, potassium and calcium amount 0.30 Mt, 0.11 Mt and 0.21 Mt, respectively. The mining stockpiles contributing most to the presence of these elements are ST1 (0.17 Mt for Al and 0.08 Mt for K) and

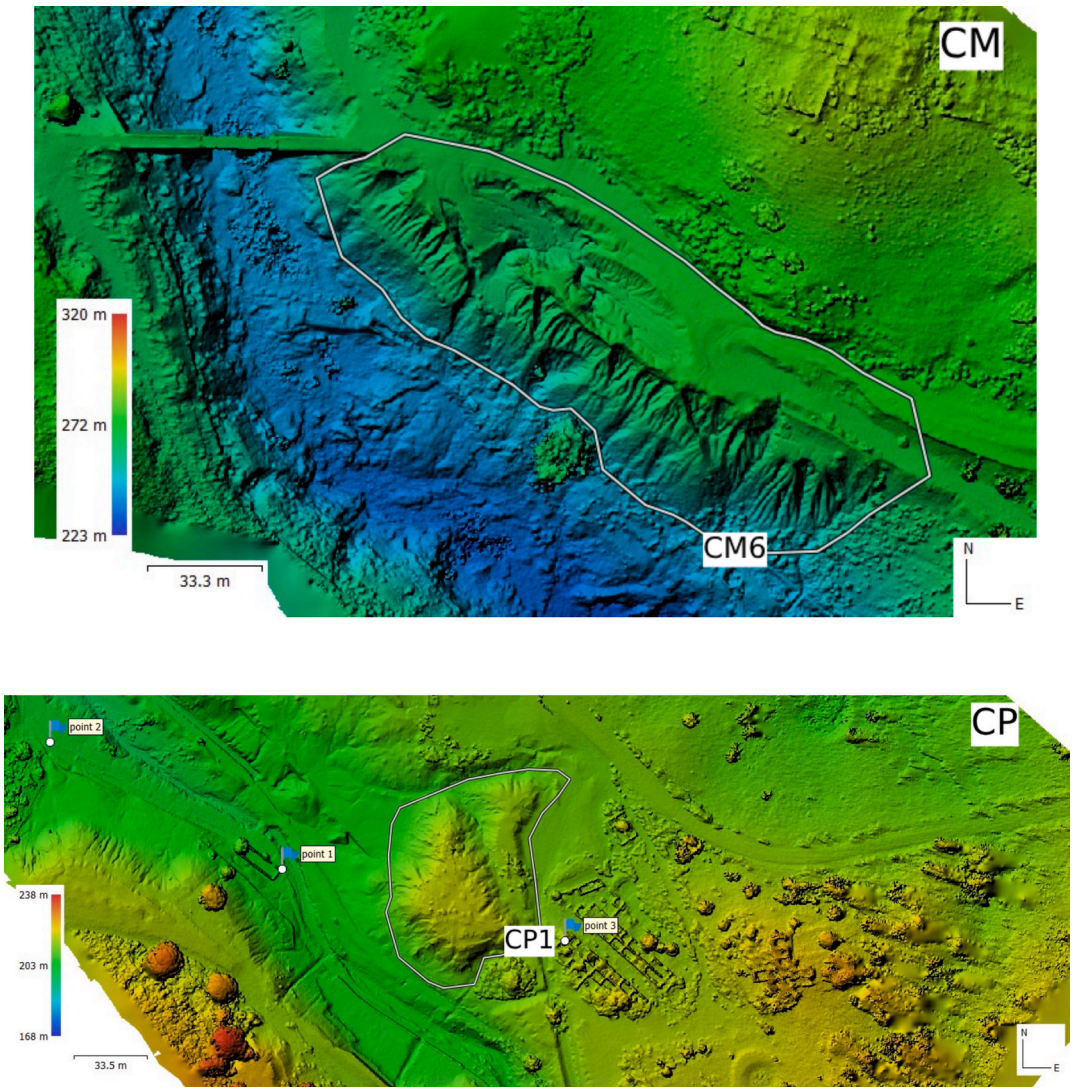

Fig. 5. (*continued*).

RT2 (0.07 Mt for Ca). In addition, the estimated total magnesium reserves amount 0.04 Mt of magnesium, 0.03 Mt sodium and 0.02 Mt titanium. All these quantities for these four elements can be considerable for a possible valorization.

It is necessary to mention the estimated reserves of the metal/metalloids As, Cu, Zn and Pb. In total, 0.06 Mt is estimated arsenic, 0.05 Mt copper, 0.09 Mt lead and 0.12 Mt zinc. The mining stockpile with the highest reserve estimates for these metals/metalloids is SC2 (0.02 Mt for As, 0.01 Mt for Cu, 0.02 Mt for Pb and 0.05 Mt for Zn). These reserves may be of interest from a raw material recovery and extraction point of view if there is a certain amount of wealth, as these metals have a wide variety of applications, both technologically and industrially.

Rare Earth elements

A key aspect to analyze involves the Rare Earth Elements (REE). The estimated masses of these elements in the different mining stockpiles are given in Table 3. As in the previous section, these estimated reserves were obtained by multiplying the masses of the mining stockpiles in Table 1 by the REE concentrations provided by ICP-OES. For light REE (La, Ce, Pr, Nd and Sm), are the most abundant (total amounts): 150 t lanthanum, 383 t cerium, 52.7 t praseodymium, 208 t neodymium, and 44 t samarium. The mining stockpiles that stand out in quantities of these elements are RT1 (36.6 t Ce, 15.7 t Nd) and SC1 (76.8 t Ce, 34.5 t Nd).

For Heavy REE (Ho, Er, Tm, Yb and Lu), the estimated masses obtained are: 8.6 t holmium, 25.2 t erbium, 3.64 t thulium. 25.3 t ytterbium, and 3.57 t lutetium. Finally, for the Medium REE (Eu, Gd, Tb, Dy), the estimated masses are: 8.97 t europium, 38.7 t gadolinium, 6.36 t terbium and 40.3 t dysprosium. Similarly, SC1 and RT1 mounds have a higher estimated quantity for both groups (see Table 3).

Based on the REE estimates, these stockpiles appear to be highly promising targets for recovery and extraction. Stockpile ST1, with an estimated 402.07 t of REE, accounts for more than 40 % of the total accumulated amount (989 t), highlighting its significant valorization potential. The high global demand for REEs has driven price increases, particularly between 2008 and 2011 (Lucas et al., 2015), although prices have shown substantial fluctuations due to market monopolization, especially for La and Ce, which reached approximately 150 USD/kg at their peak and dropped to around 15 USD/kg by 2019. In contrast, the prices of Nd and Tb have been trending upward in recent years (Patil et al., 2022).

Natural radionuclides

Although there are no specific applications, assessing the radiological composition of the samples is essential for evaluating their environmental impact. As mining activities fall under the category of NORM

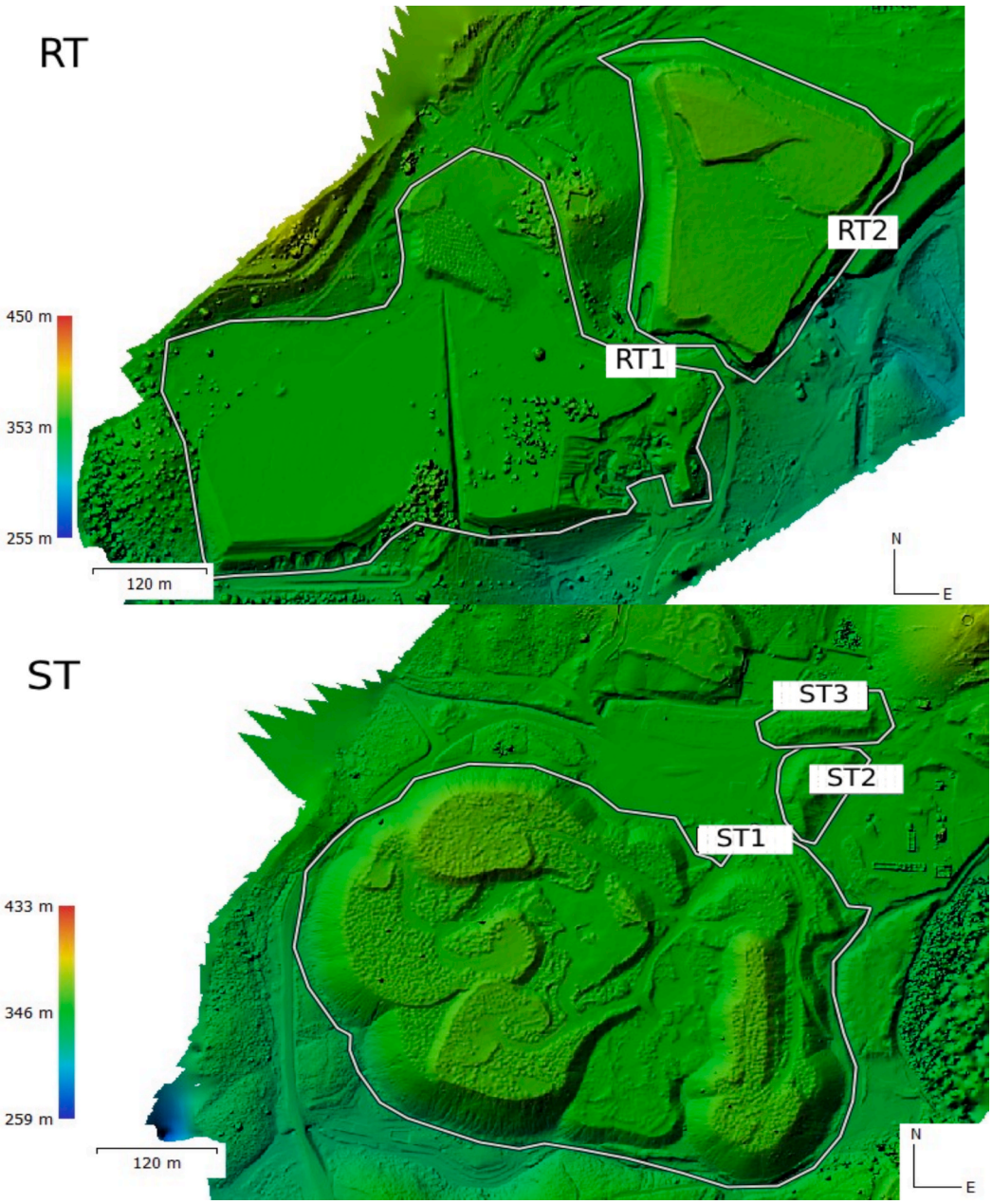

Fig. 5. (*continued*).

(Naturally Occurring Radioactive Materials), wastes produced may represent a potential radiological hazard, and consequently activity concentrations of naturally occurring radionuclides must be determined.

Activity concentrations for ^{238}U, ^{232}Th and ^{40}K obtained by gamma spectrometry are shown in Table 4, since in a previous has been demonstrated that for both ^{238}U and ^{232}Th-series radionuclides are in secular equilibrium. For ^{238}U, all mining wastes have activity concentrations for this radionuclide similar to those expected for a typical soil, 30–40 Bq kg^{-1} (Guerrero et al., 2024). For CM2, although the activity concentration is of the same order of magnitude, it doubles this value (83 ± 8 Bq kg^{-1}), although it does not pose any radiological problem. The other mining stockpiles that exceed the soil values but to a lesser extent are LA1 (57 ± 7Bq kg^{-1}) and CP1 (53 ± 8 Bq kg^{-1}).

Similarly, the activity concentrations obtained for ^{232}Th are similar to the Spanish average for undisturbed soils (41 Bq kg^{-1}; Quindos et al., 1994). The residues with the highest concentrations of this radionuclide are CP1 (46 ± 4Bq kg^{-1}), SC1 (42.0 ± 0.9Bq kg^{-1}) and ZP1 (42 ± 4Bq kg^{-1}). Finally, for the ^{40}K, the activity concentrations are also similar, the same order of magnitude, to the Spanish average, around 600 Bq kg^{-1} (Charles, 2001). The mining stockpiles with the highest concentrations of 40 K activity are CP1 (910 ± 40Bq kg^{-1}), ST1 (690 ± 30Bq kg^{-1}) and CM1 (510 ± 21Bq kg^{-1}).

Considering the measured activity concentrations in the mining stockpiles, the enhanced estimated exposure levels would not exceed the annual effective dose limit of 1 mSv y^{-1} established by the International Commission on Radiological Protection (ICRP; Wrixon, 2008). These values are also well below the exemption and clearance levels of 1000 Bq kg^{-1} for ^{238}U and ^{232}Th-series and 10000 Bq kg^{-1} for ^{40}K, defined by the Spanish Royal Decree 1029/2022 (Santos et al., 2022), which regulate exposure from Naturally Occurring Radioactive Materials (NORM). Consequently, these wastes can be regarded as non-radiologically significant and may be exempt from NORM classification. The US Environmental Protection Agency has established a threshold for equivalent radium of 370 Bq kg^{-1} so that a residue can be

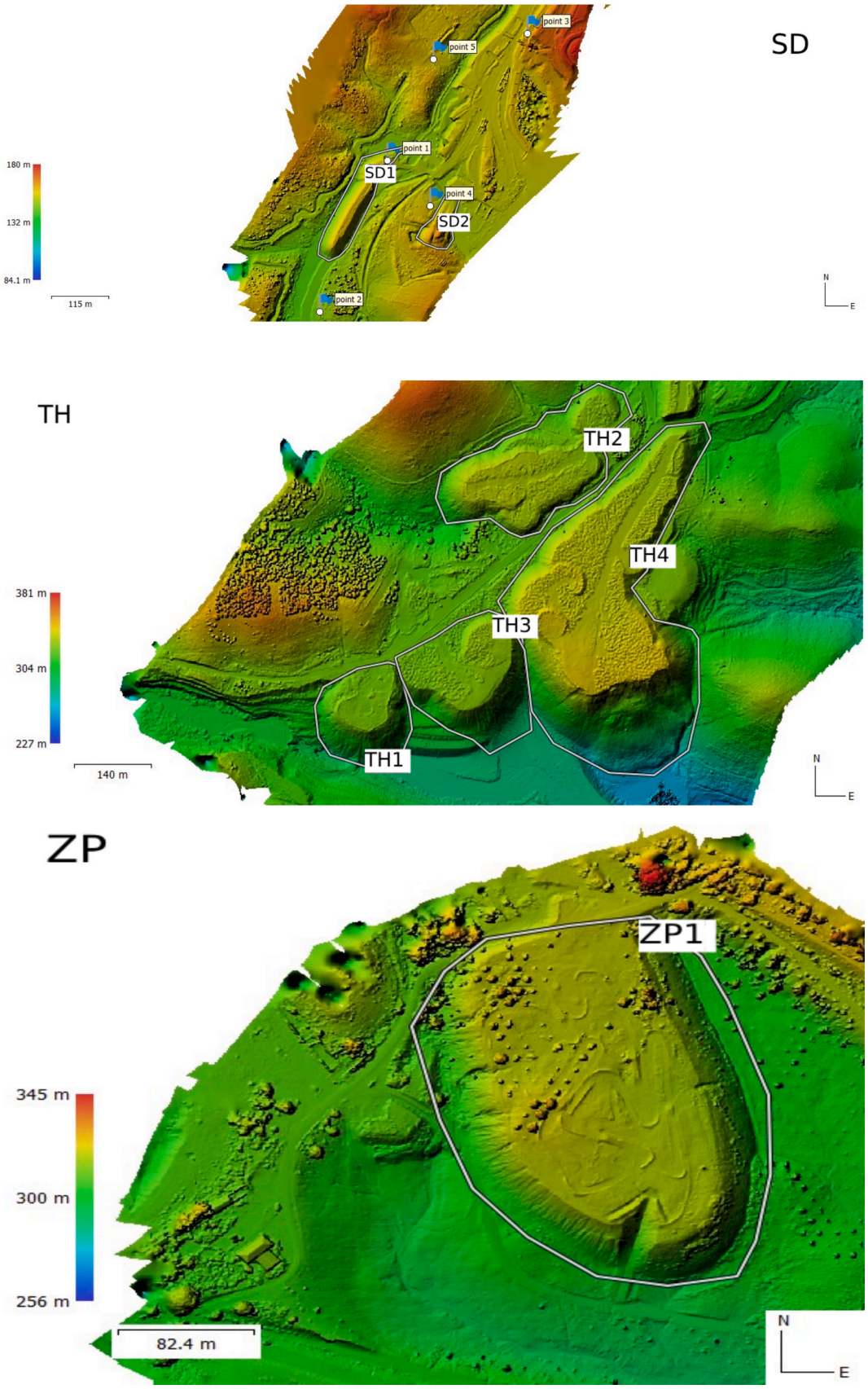

Fig. 5. (*continued*).

Table 1
Areas and volumes estimated, apparent densities obtained in the laboratory and mass in tons calculated for the different mining stockpiles.

Mining stockpile	Type of waste	Area (m^2)	Volume (m^3)	Density (kg m^{-3})	Mass (t)
CC1	Atmospheric pressure leaching waste	$6.79•10^5$	$3.61•10^6$	$1.47•10^3$	$5.31•10^6$
TH1	Leached Pyrite	$2.49•10^4$	$2.64•10^5$	$9.16•10^2$	$2.42•10^5$
TH2	Leached Pyrite	$4.95•10^4$	$4.28•10^5$	$9.60•10^2$	$4.11•10^5$
TH3	Leached Pyrite	$4.12•10^4$	$3.87•10^5$	$1.02•10^3$	$3.94•10^5$
TH4	Leached Pyrite	$1.36•10^5$	$2.59•10^6$	$9.80•10^2$	$2.54•10^6$
LA1	Leached Pyrite	$5.28•10^4$	$7.94•10^4$	$1.25•10^3$	$9.93•10^4$
LA2	Roasted Pyrite	$5.14•10^4$	$8.21•10^4$	$1.58•10^3$	$1.30•10^5$
CM1	Slag	$2.57•10^3$	$9.11•10^3$	$2.18•10^3$	$1.98•10^4$
CM2	Slag	$2.98•10^3$	$6.63•10^3$	$2.16•10^3$	$1.43•10^4$
CM3	Slag	$2.28•10^3$	$7.47•10^3$	$2.15•10^3$	$1.61•10^4$
CM4	Slag	$1.65•10^3$	$3.10•10^3$	$2.15•10^3$	$6.65•10^3$
CM5	Slag	$1.85•10^4$	$8.66•10^4$	$2.16•10^3$	$1.87•10^5$
CM6	Roasted Pyrite	$1.00•10^4$	$4.08•10^4$	$1.22•10^3$	$4.97•10^4$
ST1	Leached Pyrite	$1.89•10^5$	$2.94•10^6$	$1.23•10^3$	$3.60•10^6$
ST2	Leached Pyrite	$6.21•10^3$	$1.98•10^4$	$1.21•10^3$	$2.39•10^4$
ST3	Leached Pyrite	$6.20•10^3$	$1.50•10^4$	$1.22•10^3$	$1.83•10^4$
ZP1	Leached Pyrite	$4.54•10^4$	$3.84•10^5$	$1.14•10^3$	$4.40•10^5$
RT1	Jarosite pond	$1.45•10^5$	$6.70•10^5$	$1.15•10^3$	$7.72•10^5$
RT2	Slag	$6.99•10^4$	$8.90•10^5$	$1.99•10^3$	$1.77•10^6$
SC1	Roasted Pyrite	$2.20•10^5$	$2.42•10^6$	$1.27•10^3$	$3.67•10^6$
SC2	Floated Pyrite	$1.98•10^5$	$2.44•10^6$	$1.50•10^3$	$3.07•10^6$
CP1	Leached Pyrite	$5.61•10^3$	$2.00•10^4$	$9.78•10^2$	$1.96•10^4$
CA1	Leached Pyrite	$2.26•10^4$	$9.21•10^4$	$1.51•10^3$	$1.40•10^5$
SD1	Slag	$1.27•10^4$	$6.99•10^4$	$1.89•10^3$	$1.32•10^5$
SD2	Slag	$5.04•10^3$	$1.61•10^4$	$1.88•10^3$	$3.03•10^4$
HE1	Leached Pyrite	$1.64•10^4$	$3.47•10^4$	$9.73•10^2$	$3.38•10^4$
HE2	Leached Pyrite	$4.55•10^4$	$1.43•10^5$	$1.16•10^3$	$1.65•10^5$
Total	–	**$2.06•10^6$**	**$1.77•10^7$**	–	**$2.33•10^7$**

used in any application without any restrictions (Eke et al., 2024).

It is important to highlight that each mining site has different activity concentration values for the same residue. This variability can be attributed to differences in the specific mineralogical processes associated with each deposit, or the storage conditions, especially if external environmental factors have altered the materials.

Valorization diagnosis

The waste dumps in the IPB represent a significant environmental concern (Pérez-López et al., 2007). Remediation efforts could be mitigated if these mining waste stockpiles in this area, or portions of them, are exploited for their economic potential. Such initiatives are consistent with circular economy principles, promoting efficient material recovery and making use of the inherent properties and characteristics of the wastes. Considering the substantial volumes of mining stockpiles estimated in this study, various strategies for their recovery are proposed.

The case of SC1 is particularly notable because, as mentioned earlier, it contains 1.54 Mt of Fe, representing a significant opportunity for valorization. Previous investigations at this mine have indicated that the waste is predominantly hematite (64 %), making it suitable for reuse (Ramírez-Pérez et al., 2025). Studies suggest that this hematite could be employed in the production of iron oxide pigments (Liu & Zheng, 2011). By substituting La^{3+} ions into the hematite lattice ($Fe_{2-x}La_xO_3$) through a polymeric complex method at high temperatures (~1000 °C), pigments with various color tones can be synthesized (Bhuiyan et al., 2007).

Additionally, this waste can serve as an iron source in clinker production. For instance, roasted pyrite containing 85 % hematite has been used in Portland cement mortars at 2.5–6 % incorporation. Over a six-month period, evaluations of physical, chemical, and mechanical properties showed that the mortars achieved a compressive strength of 43.7 MPa after 28 days, comparable to conventional type 2 cement. Leaching tests also confirmed that no toxic metals or metalloids were released, indicating no environmental risk (Alp et al., 2009). Assuming an effective utilization of 60–70 % of this waste, the potentially usable amount would be approximately 2.5–3 Mt. Similar considerations apply to LA2 and CM6, with Fe contents estimated at around 0.04 Mt and 0.03 Mt, respectively.

Given the estimated concentrations of metals and metalloids such as Pb and Zn, targeted extraction or valorization techniques are required for these elements. The estimated reserves in RT2 (slag waste) amount to approximately 0.03 Mt of Zn, while SC1 contains around 0.04 Mt of Pb, representing significant quantities for potential valorization. A recent study by Li et al. (2024) demonstrated the successful conversion of waste with high Pb and Zn content into useful products through geopolymerization, which could have applications in the construction industry. By curing the geopolymer for 28 days, incorporating 5 % gypsum, and activating with 10 M NaOH, the resulting material achieved an unconfined compressive strength exceeding 24.1 MPa (Li et al., 2024).

Given the estimated concentrations of REEs in the mining wastes, particularly in ST1 (approximately 400 t), it is important to evaluate the economic potential of their extraction. Rare Earth Elements such as lanthanum, cerium, neodymium, and europium possess unique properties, including high thermal resistance and excellent electrical

Table 2
Major elements estimated masses (metric tons) for each mining stockpile studied. Total estimated reserves are also included.

Mining stockpile	Mg	Al	K	Ca	Fe	Zn	S	Pb	Cu	Ti	As	Na	Si
CC1	$2.6•10^3$	$1.5•10^4$	$3.2•10^3$	$9.9•10^4$	$4.6•10^3$	$6.9•10^3$	$7.2•10^5$	$2.2•10^4$	$1.6•10^4$	$4.2•10^3$	$8.0•10^3$	$4.8•10^3$	$2.2•10^5$
TH1	$3.4•10^2$	$4.3•10^3$	$9.2•10^2$	$9.7•10^1$	$3.7•10^4$	$8.5•10^2$	$3.6•10^4$	$3.1•10^2$	$5.3•10^2$	$1.7•10^2$	$3.4•10^2$	$7.3•10^1$	$7.5•10^3$
LA1	$2.0•10^1$	$7.7•10^2$	$3.3•10^2$	$9.9•10^0$	$1.4•10^3$	$9.9•10^0$	$1.1•10^3$	$4.4•10^3$	$9.9•10^0$	$4.3•10^2$	$2.3•10^2$	$5.0•10^1$	$3.8•10^4$
LA2	$1.3•10^1$	$7.3•10^2$	$2.7•10^2$	$6.5•10^0$	$4.1•10^4$	$9.1•10^1$	$1.4•10^3$	$2.7•10^3$	$1.0•10^2$	$1.7•10^2$	$6.4•10^2$	$3.9•10^1$	$6.8•10^3$
CM1	$1.1•10^2$	$2.7•10^2$	$1.7•10^2$	$1.7•10^2$	$5.3•10^3$	$8.3•10^1$	$1.1•10^2$	$1.8•10^1$	$1.3•10^2$	$2.2•10^1$	$1.2•10^2$	$6.7•10^1$	$1.3•10^3$
CM2	$5.9•10^1$	$1.6•10^2$	$5.2•10^1$	$3.9•10^2$	$5.0•10^3$	$5.0•10^2$	$1.1•10^2$	$4.3•10^1$	$5.7•10^1$	$7.2•10^0$	$7.3•10^1$	$1.1•10^2$	$2.1•10^3$
CM6	$1.5•10^1$	$1.3•10^2$	$2.5•10^1$	$1.3•10^2$	$2.9•10^4$	$2.5•10^1$	$6.3•10^2$	$2.0•10^2$	$3.5•10^1$	$5.0•10^0$	$2.7•10^2$	$5.0•10^1$	$1.2•10^3$
ST1	$7.2•10^3$	$1.7•10^5$	$7.9•10^4$	$4.0•10^3$	$3.8•10^5$	$7.2•10^2$	$3.8•10^5$	$7.2•10^2$	$7.2•10^2$	$8.7•10^3$	$7.2•10^2$	$1.1•10^4$	$8.8•10^5$
ST2	$2.9•10^1$	$3.5•10^2$	$1.6•10^2$	$7.2•10^0$	$6.9•10^3$	$3.8•10^1$	$4.8•10^3$	$9.6•10^0$	$4.8•10^2$	$1.4•10^1$	$1.2•10^1$	$4.1•10^1$	$2.0•10^3$
ST3	$1.8•10^1$	$3.1•10^2$	$1.4•10^2$	$7.3•10^0$	$3.4•10^3$	$6.6•10^1$	$3.5•10^3$	$9.1•10^0$	$3.8•10^1$	$5.5•10^0$	$7.3•10^0$	$8.4•10^1$	$2.7•10^3$
ZP1	$4.4•10^2$	$1.2•10^4$	$4.7•10^3$	$4.4•10^1$	$3.2•10^4$	$1.8•10^2$	$4.0•10^4$	$3.5•10^3$	$2.6•10^2$	$1.4•10^3$	$2.6•10^2$	$9.2•10^2$	$1.3•10^5$
RT1	$4.0•10^3$	$1.4•10^4$	$2.1•10^3$	$7.7•10^1$	$1.2•10^5$	$1.5•10^2$	$4.6•10^3$	$3.9•10^2$	$1.5•10^2$	$5.4•10^2$	$8.5•10^2$	$7.7•10^1$	$2.4•10^5$
RT2	$6.7•10^3$	$2.1•10^4$	$3.4•10^3$	$6.6•10^4$	$6.9•10^5$	$3.2•10^4$	$3.2•10^4$	$3.5•10^3$	$7.4•10^3$	$7.1•10^2$	$1.8•10^2$	$4.1•10^3$	$2.3•10^5$
SC1	$7.1•10^3$	$2.1•10^4$	$4.8•10^3$	$2.6•10^4$	$1.5•10^6$	$3.2•10^4$	$4.3•10^4$	$3.3•10^4$	$7.3•10^3$	$7.3•10^3$	$2.4•10^4$	$3.2•10^3$	$1.2•10^5$
SC2	$9.6•10^3$	$2.3•10^4$	$3.4•10^3$	$1.1•10^4$	$5.8•10^5$	$4.8•10^4$	$1.6•10^6$	$2.2•10^4$	$1.3•10^4$	$5.0•10^2$	$2.1•10^4$	$8.4•10^2$	$5.1•10^4$
CP1	$3.9•10^0$	$6.2•10^2$	$4.4•10^2$	$3.9•10^0$	$1.4•10^3$	$2.0•10^0$	$1.3•10^3$	$2.2•10^1$	$3.9•10^0$	$8.6•10^1$	$5.9•10^0$	$3.7•10^1$	$3.3•10^3$
CA1	$2.1•10^2$	$3.7•10^3$	$1.7•10^3$	$3.6•10^2$	$2.0•10^4$	$1.4•10^1$	$1.6•10^4$	$2.8•10^1$	$3.2•10^2$	$2.4•10^2$	$2.8•10^1$	$3.4•10^2$	$1.2•10^4$
SD1	$5.4•10^2$	$4.1•10^3$	$8.2•10^2$	$6.8•10^3$	$3.4•10^3$	$2.6•10^2$	$1.4•10^4$	$7.8•10^2$	$1.3•10^1$	$2.6•10^2$	$2.8•10^2$	$9.5•10^2$	$1.7•10^4$
HE1	$3.4•10^0$	$2.0•10^1$	$6.8•10^0$	$3.4•10^0$	$3.1•10^2$	$3.4•10^0$	$1.4•10^3$	$1.2•10^3$	$3.4•10^0$	$2.4•10^1$	$1.4•10^1$	$3.4•10^0$	$1.1•10^4$
Total	**$3.9•10^4$**	**$3.0•10^5$**	**$1.1•10^5$**	**$2.1•10^5$**	**$3.5•10^6$**	**$1.2•10^5$**	**$2.9•10^6$**	**$9.4•10^4$**	**$4.6•10^4$**	**$2.5•10^4$**	**$5.7•10^4$**	**$2.7•10^4$**	**$2.0•10^6$**

Table 3
Rare Earth Elements estimated masses in metric tons for each mining stockpile studied. Total estimated reserves are also included.

Mining stockpile	La	Ce	Pr	Nd	Sm	Eu	Gd	Tb	Dy	Ho	Er	Tm	Yb	Lu
CC1	$3.1\cdot10^{1}$	$6.5\cdot10^{1}$	$8.0\cdot10^{0}$	$3.0\cdot10^{1}$	$5.8\cdot10^{0}$	$2.0\cdot10^{0}$	$5.3\cdot10^{0}$	$1.1\cdot10^{0}$	$6.9\cdot10^{0}$	$1.6\cdot10^{0}$	$4.2\cdot10^{0}$	$5.3\cdot10^{-1}$	$4.2\cdot10^{0}$	$5.3\cdot10^{-1}$
TH1	$2.7\cdot10^{0}$	$6.0\cdot10^{0}$	$7.5\cdot10^{-1}$	$2.8\cdot10^{0}$	$5.8\cdot10^{-1}$	$6.5\cdot10^{-2}$	$5.1\cdot10^{-1}$	$7.3\cdot10^{-2}$	$3.9\cdot10^{-1}$	$9.7\cdot10^{-2}$	$2.7\cdot10^{-1}$	$2.4\cdot10^{-2}$	$2.4\cdot10^{-1}$	$2.4\cdot10^{-2}$
LA1	$2.2\cdot10^{0}$	$3.5\cdot10^{0}$	$4.1\cdot10^{-1}$	$1.4\cdot10^{0}$	$1.8\cdot10^{-1}$	$4.7\cdot10^{-2}$	$1.8\cdot10^{-1}$	$3.0\cdot10^{-2}$	$2.3\cdot10^{-1}$	$5.0\cdot10^{-2}$	$1.4\cdot10^{-1}$	$2.0\cdot10^{-2}$	$1.5\cdot10^{-1}$	$2.0\cdot10^{-2}$
LA2	$8.3\cdot10^{-1}$	$1.5\cdot10^{0}$	$1.7\cdot10^{-1}$	$5.7\cdot10^{-1}$	$7.8\cdot10^{-2}$	$2.1\cdot10^{-2}$	$9.1\cdot10^{-2}$	$1.3\cdot10^{-2}$	$1.0\cdot10^{-1}$	$2.6\cdot10^{-2}$	$6.5\cdot10^{-2}$	$6.5\cdot10^{-3}$	$6.5\cdot10^{-2}$	$6.5\cdot10^{-3}$
CM1	$3.1\cdot10^{-1}$	$5.8\cdot10^{-1}$	$6.7\cdot10^{-2}$	$2.4\cdot10^{-1}$	$4.6\cdot10^{-2}$	$1.1\cdot10^{-2}$	$4.4\cdot10^{-2}$	$5.9\cdot10^{-3}$	$3.2\cdot10^{-2}$	$5.9\cdot10^{-3}$	$1.8\cdot10^{-2}$	$2.0\cdot10^{-3}$	$1.8\cdot10^{-2}$	$2.0\cdot10^{-3}$
CM2	$6.5\cdot10^{-2}$	$2.1\cdot10^{-1}$	$3.0\cdot10^{-2}$	$1.2\cdot10^{-1}$	$2.7\cdot10^{-2}$	$7.0\cdot10^{-3}$	$3.3\cdot10^{-2}$	$5.7\cdot10^{-3}$	$3.4\cdot10^{-2}$	$7.2\cdot10^{-3}$	$2.0\cdot10^{-2}$	$2.9\cdot10^{-3}$	$1.9\cdot10^{-2}$	$2.9\cdot10^{-3}$
CM6	$1.4\cdot10^{-1}$	$2.3\cdot10^{-1}$	$2.5\cdot10^{-2}$	$9.0\cdot10^{-2}$	$2.0\cdot10^{-2}$	$4.5\cdot10^{-3}$	$1.5\cdot10^{-2}$	$2.5\cdot10^{-3}$	$9.9\cdot10^{-3}$	$2.5\cdot10^{-3}$	$9.9\cdot10^{-3}$	$2.5\cdot10^{-3}$	$5.0\cdot10^{-3}$	$2.5\cdot10^{-3}$
ST1	$4.3\cdot10^{1}$	$1.5\cdot10^{2}$	$2.3\cdot10^{1}$	$9.5\cdot10^{1}$	$2.1\cdot10^{1}$	$3.1\cdot10^{0}$	$1.7\cdot10^{1}$	$2.9\cdot10^{0}$	$1.8\cdot10^{1}$	$4.0\cdot10^{0}$	$1.2\cdot10^{1}$	$1.8\cdot10^{0}$	$1.2\cdot10^{1}$	$1.8\cdot10^{0}$
ST2	$1.4\cdot10^{-2}$	$5.0\cdot10^{-2}$	$9.6\cdot10^{-3}$	$6.0\cdot10^{-2}$	$2.6\cdot10^{-2}$	$4.3\cdot10^{-3}$	$4.3\cdot10^{-2}$	$9.6\cdot10^{-3}$	$6.0\cdot10^{-2}$	$1.4\cdot10^{-2}$	$4.6\cdot10^{-2}$	$4.8\cdot10^{-3}$	$4.3\cdot10^{-2}$	$7.2\cdot10^{-1}$
ST3	$1.1\cdot10^{-2}$	$4.6\cdot10^{-2}$	$1.1\cdot10^{-2}$	$7.0\cdot10^{-2}$	$3.1\cdot10^{-2}$	$3.3\cdot10^{-3}$	$3.1\cdot10^{-2}$	$5.5\cdot10^{-3}$	$4.6\cdot10^{-2}$	$9.1\cdot10^{-3}$	$3.3\cdot10^{-2}$	$5.5\cdot10^{-3}$	$3.3\cdot10^{-2}$	$5.5\cdot10^{-2}$
ZP1	$8.4\cdot10^{-1}$	$3.3\cdot10^{0}$	$6.6\cdot10^{-1}$	$3.4\cdot10^{0}$	$1.6\cdot10^{0}$	$4.0\cdot10^{-1}$	$2.0\cdot10^{0}$	$3.5\cdot10^{-1}$	$2.2\cdot10^{0}$	$5.3\cdot10^{-1}$	$1.4\cdot10^{0}$	$2.2\cdot10^{-1}$	$1.5\cdot10^{0}$	$2.2\cdot10^{-1}$
RT1	$1.7\cdot10^{1}$	$3.7\cdot10^{1}$	$4.3\cdot10^{0}$	$1.6\cdot10^{1}$	$3.7\cdot10^{0}$	$5.4\cdot10^{-1}$	$2.7\cdot10^{0}$	$3.9\cdot10^{-1}$	$2.1\cdot10^{0}$	$3.9\cdot10^{-1}$	$1.2\cdot10^{0}$	$2.3\cdot10^{-1}$	$1.5\cdot10^{0}$	$2.3\cdot10^{-1}$
RT2	$1.4\cdot10^{1}$	$2.8\cdot10^{1}$	$3.4\cdot10^{0}$	$1.4\cdot10^{1}$	$1.6\cdot10^{0}$	$5.7\cdot10^{-1}$	$2.3\cdot10^{0}$	$3.5\cdot10^{-1}$	$2.3\cdot10^{0}$	$5.3\cdot10^{-1}$	$1.2\cdot10^{0}$	$1.8\cdot10^{-1}$	$1.2\cdot10^{0}$	$1.8\cdot10^{-1}$
SC1	$3.2\cdot10^{1}$	$7.7\cdot10^{1}$	$9.6\cdot10^{0}$	$3.5\cdot10^{1}$	$6.5\cdot10^{0}$	$1.1\cdot10^{0}$	$4.9\cdot10^{0}$	$6.7\cdot10^{-1}$	$3.5\cdot10^{0}$	$6.7\cdot10^{-1}$	$2.0\cdot10^{0}$	$2.7\cdot10^{-1}$	$1.9\cdot10^{0}$	$2.7\cdot10^{-1}$
SC2	$1.9\cdot10^{0}$	$3.5\cdot10^{0}$	$1.2\cdot10^{0}$	$6.7\cdot10^{0}$	$2.5\cdot10^{0}$	$8.5\cdot10^{-1}$	$2.9\cdot10^{0}$	$4.0\cdot10^{-1}$	$3.2\cdot10^{0}$	$5.9\cdot10^{-1}$	$1.8\cdot10^{0}$	$2.9\cdot10^{-1}$	$1.7\cdot10^{0}$	$2.2\cdot10^{-1}$
CP1	$7.1\cdot10^{-1}$	$1.4\cdot10^{0}$	$1.6\cdot10^{-1}$	$5.0\cdot10^{-1}$	$7.6\cdot10^{-2}$	$1.6\cdot10^{-2}$	$7.1\cdot10^{-2}$	$1.2\cdot10^{-2}$	$7.8\cdot10^{-2}$	$1.6\cdot10^{-2}$	$5.1\cdot10^{-2}$	$7.8\cdot10^{-3}$	$5.1\cdot10^{-2}$	$5.9\cdot10^{-3}$
CA1	$2.5\cdot10^{0}$	$4.9\cdot10^{0}$	$5.7\cdot10^{-1}$	$2.3\cdot10^{0}$	$4.1\cdot10^{-1}$	$1.2\cdot10^{-1}$	$3.8\cdot10^{-1}$	$5.6\cdot10^{-2}$	$3.8\cdot10^{-1}$	$7.0\cdot10^{-2}$	$2.4\cdot10^{-1}$	$2.8\cdot10^{-2}$	$2.1\cdot10^{-1}$	$2.8\cdot10^{-2}$
SD1	$1.5\cdot10^{0}$	$3.0\cdot10^{0}$	$3.7\cdot10^{-1}$	$1.3\cdot10^{0}$	$3.0\cdot10^{-1}$	$8.3\cdot10^{-2}$	$2.8\cdot10^{-1}$	$4.0\cdot10^{-2}$	$2.4\cdot10^{-1}$	$4.0\cdot10^{-2}$	$1.1\cdot10^{-1}$	$1.3\cdot10^{-2}$	$1.2\cdot10^{-1}$	$1.3\cdot10^{-2}$
HE1	$1.4\cdot10^{-1}$	$1.9\cdot10^{-1}$	$2.0\cdot10^{-2}$	$6.1\cdot10^{-2}$	$1.0\cdot10^{-2}$	$3.0\cdot10^{-3}$	$1.0\cdot10^{-2}$	$1.7\cdot10^{-3}$	$1.0\cdot10^{-2}$	$1.7\cdot10^{-3}$	$6.8\cdot10^{-3}$	$1.7\cdot10^{-3}$	$6.8\cdot10^{-3}$	$1.7\cdot10^{-3}$
Total	$\mathbf{1.5\cdot10^{2}}$	$\mathbf{3.8\cdot10^{2}}$	$\mathbf{5.3\cdot10^{1}}$	$\mathbf{2.1\cdot10^{2}}$	$\mathbf{4.4\cdot10^{1}}$	$\mathbf{9.0\cdot10^{0}}$	$\mathbf{3.9\cdot10^{1}}$	$\mathbf{6.4\cdot10^{0}}$	$\mathbf{4.0\cdot10^{1}}$	$\mathbf{8.6\cdot10^{0}}$	$\mathbf{2.5\cdot10^{1}}$	$\mathbf{3.6\cdot10^{0}}$	$\mathbf{2.5\cdot10^{1}}$	$\mathbf{3.6\cdot10^{0}}$

Table 4
Activity concentrations for ^{238}U, ^{232}Th and ^{40}K in Bq kg^{-1} for each mining dump sample studied.

Mining stockpile	^{238}U	^{232}Th	^{40}K
CC1	5 ± 8	21.6 ± 1.5	9 ± 9
TH1	15 ± 3	14.0 ± 2.1	270 ± 14
LA1	57 ± 7	20 ± 3	107 ± 10
LA2	10 ± 3	7.1 ± 1.7	67 ± 7
CM1	12 ± 3	17.3 ± 1.2	510 ± 21
CM2	83 ± 9	9.8 ± 1.3	96 ± 5
CM6	10 ± 3	2.1 ± 0.9	11 ± 3
ST1	27 ± 6	31 ± 4	690 ± 30
ST2	29 ± 4	18.5 ± 1.8	227 ± 11
ST3	18 ± 4	19 ± 3	211 ± 13
ZP1	35 ± 6	42 ± 4	395 ± 22
RT1	30 ± 4	35 ± 3	88 ± 8
RT2	13.1 ± 1.9	9.5 ± 1.0	48 ± 4
SC1	26.8 ± 2.4	42.0 ± 0.9	50 ± 3
SC2	15.2 ± 1.3	2.9 ± 0.3	19.8 ± 1.7
CP1	53 ± 8	46 ± 4	910 ± 40
CA1	16 ± 4	16.7 ± 2.2	486 ± 23
SD1	21.5 ± 2.3	12.0 ± 1.4	57 ± 4
HE1	6 ± 9	33 ± 4	5 ± 12
Mean	25 ± 5	20.9 ± 2.2	224 ± 13

conductivity, making them critical for a wide range of technologies. These include mobile phones, lighting systems, magnets, batteries, and wind turbines, as well as everyday products such as LEDs, fiber optics, and compact fluorescent lamps. REEs are also used as catalysts, in air pollution control, and as polishing agents for high-quality optical glass. The demand for these elements has increased significantly over time, expanding their range of applications (Fakolade et al., 2024; Balaram, 2019). Moreover, REEs have contributed to the study and monitoring of earthquakes (Mouslopoulou et al., 2011). Tunsu and colleagues developed a leaching method for REE extraction, employing 4 M HCl for 24 h at 20 °C, achieving a 95 % recovery of europium. The study also indicated that increasing the temperature could enhance the extraction efficiency of other REEs, such as cerium and gadolinium (Tunsu et al., 2014).

However, any valorization or reuse initiative must be carefully evaluated considering the environmental risks associated with these mining wastes. In particular, residues rich in sulfides and jarosite may generate acid mine drainage (AMD) when exposed to oxidation and rainfall, leading to metal mobilization and soil or water contamination (Nieto et al., 2007; Alam et al., 2012). Moreover, the unconsolidated nature and steep slopes of several dumps (e.g., Tharsis, Cueva de la Mora) increase their susceptibility to erosion and mass wasting processes (Martín-Velázquez et al., 2022).

To minimize these risks, integrated management strategies should be implemented prior to or concurrently with valorization efforts. These could include surface stabilization and revegetation, installation of drainage and containment systems to control runoff, and covering or encapsulation of reactive materials to limit oxygen and water infiltration (Navarro-Ramos et al., 2022; Shabalala et al., 2014; Terrones-Saeta et al., 2021). Coupling these preventive measures with periodic environmental monitoring would ensure that resource recovery initiatives proceed within a sustainable and safe framework.

Conclusions

This research provides a comprehensive assessment of abandoned mining wastes in the Iberian Pyrite Belt (IPB), integrating geomatic, geochemical, and radiological analyses. The results obtained allow for a better understanding of the environmental status and recovery potential of these legacy sites. The main conclusions are summarized as follows:

1. This study successfully achieved the first volumetric inventory and quantitative assessment of mining wastes across 12 mines in the

Iberian Pyrite Belt (IPB). Unmanned Aerial Vehicles (UAVs) were used to generate high-resolution Digital Elevation Models (DEMs) for accurate waste estimation. The total waste reserves were estimated to be 23.3 Mt ($1.77 \cdot 10^7$ m^3).

2. This research thereby fills a critical knowledge gap by providing, for the first time, a quantitative assessment of waste volumes and metal reserves in the IPB. Moreover, the UAV-based methodology demonstrated here offers a replicable framework for mining waste inventories in other historical mining districts worldwide.
3. The integrated geochemical characterization revealed substantial reserves of Fe (3.5 Mt), S (2.86 Mt), and Si (1.96 Mt), as well as economically significant concentrations of Zn, Pb, Cu, and As. In addition, a total of about 990 t of Rare Earth Elements (REEs) were identified, with the ST1 stockpile accounting for approximately 40 % of the total, highlighting its strong potential for valorization within circular economy frameworks.
4. The analysis of natural radionuclides showed activity concentrations comparable to those in non-contaminated soils, indicating that these residues do not pose significant radiological risks and could potentially be exempted from NORM classification.
5. Future research should focus on detailed techno-economic and environmental feasibility assessments to evaluate specific valorization pathways for Fe, Pb, Zn, and REE rich residues, contributing to sustainable resource recovery and improved mine waste management and remediation strategies.

CRediT authorship contribution statement

Juan Antonio Ramírez-Pérez: Writing – review & editing, Writing – original draft, Software, Methodology, Investigation, Formal analysis, Data curation, Conceptualization. **Felipe Jesús González Barrionuevo:** Writing – review & editing, Visualization, Validation, Supervision, Software, Resources, Methodology, Investigation, Data curation, Conceptualization. **Manuel Jesús Gázquez-González:** Writing – review & editing, Visualization, Validation, Supervision, Methodology, Investigation, Data curation, Conceptualization. **Reinaldo Sáez Ramos:** Writing – review & editing, Validation, Supervision, Project administration, Methodology, Investigation, Formal analysis, Data curation, Conceptualization. **Juan Pedro Bolívar:** Writing – review & editing, Visualization, Validation, Supervision, Software, Resources, Project administration, Methodology, Investigation, Funding acquisition, Formal analysis, Conceptualization.

Declaration of competing interest

The authors declare that they have no known competing financial interests or personal relationships that could have appeared to influence the work reported in this paper.

Acknowledgements

This research received support from the Spanish State Agency through the project “Diagnosis and proposals for the environmental recovery of areas impacted by industrial and mining activities: Implications for the Huelva estuary (RESTOREHU)” (Ref.: TED2021-130361B-I00), as well as from grants PID2020-116461RB-C21 and PID2020-116461RA-C22, funded by MICIU/AEI/10.13039/501100011033.

References

Abah, M.A., Oladosu, M.A., Eke, S.C., Nwaka, E.N., Osuji, I.D., Muhammad, A.B., Aanu, B.E., 2025. Life Cycle Assessment of Bioenergy Systems versus Fossil fuel Alternatives: Insights for Sustainable Energy Transitions in Nigeria. Trends in Ecological and Indoor Environmental Engineering 3 (2), 46–59.

Abdulrahman, F.H., Kattan, R.A., Gilyana, S.M., 2020. A Comparison between Unmanned Aerial Vehicle and Aerial Survey acquired in Separate Dates for the production of Orthophotos. Journal of Duhok University 23 (2), 52–66.

Ajayi, O.G., Salubi, A.A., Angbas, A.F., Odigure, M.G., 2017. Generation of accurate digital elevation models from UAV acquired low percentage overlapping images. Int. J. Remote Sens. 38 (8–10), 3113–3134.

Ajayi, O.G., Oyeboade, T.O., Samaila-Ija, H.A., Adewale, T.J., 2020. Development of a UAV-based system for the semi-automatic estimation of the volume of earthworks. Reports on Geodesy and Geoinformatics 110, 21–28.

Alam, R., Shang, J.Q., Cheng, X., 2012. Optimization of digestion parameters for analysing the total sulphur of mine tailings by inductively coupled plasma optical emission spectrometry. Environ. Monit. Assess. 184, 3373–3387.

Alp, İ.B.R.A.H.İ.M., Deveci, H.A.C.I., Yazıcı, E.Y., Türk, T.U.Ğ.B.A., Süngün, Y.H., 2009. Potential use of pyrite cinders as raw material in cement production: results of industrial scale trial operations. J. Hazard. Mater. 166 (1), 144–149.

Álvarez-Valero, A.M., Sáez, R., Pérez-López, R., Delgado, J., Nieto, J.M., 2009. Evaluation of heavy metal bio-availability from Almagrera pyrite-rich tailings dam (Iberian Pyrite Belt, SW Spain) based on a sequential extraction procedure. J. Geochem. Explor. 102 (2), 87–94.

Balaram, V., 2019. Rare earth elements: a review of applications, occurrence, exploration, analysis, recycling, and environmental impact. Geosci. Front. 10 (4), 1285–1303.

Barba-Lobo, A., Mosqueda, F., Bolívar, J.P., 2021. An upgraded lab-based method to determine natural γ-ray emitters in NORM samples by using Ge detectors. Measurement 186, 110153.

Bhuiyan, T.I., Nakanishi, M., Kusano, Y., Fujii, T., Takada, J., Ikeda, Y., 2007. Synthesis, morphology and color tone properties of the lanthanum substituted hematite. Mater. Lett. 61 (17), 3774–3777.

Charles, M., 2001. UNSCEAR Report 2000: sources and effects of ionizing radiation.

de Andrade Lima, L.R.P., Bernardez, L.A., 2011. Characterization of the lead smelter slag in Santo Amaro, Bahia. Brazil. Journal of Hazardous Materials 189 (3), 692–699.

Eftekhari, N., Kargar, M., Zamin, F. R., Rastakhiz, N., & Manafi, Z., 2020. A Review on Various Aspects of Jarosite and Its Utilization Potentials. In Annales de Chimie Science des Matériaux (Vol. 44, No. 1).

Eke, B.C., Akomolafe, I.R., Ukewuihe, U.M., Onyenegecha, C.P., 2024. Assessment of radiation hazard indices due to natural radionuclides in soil samples from Imo State University, Owerri. Nigeria. Environmental Health Insights 18, 11786302231224581.

Fakolade, R.O., Ikhane, P.R., Hao, Q., Ajibade, O.M., Olisa, O.G., Oyebolu, O.O., 2024. REE signatures in quaternary deposits: implication for provenance and economic potentials. Discover Environment 2 (1), 96.

Guerrero, J.L., Barba-Lobo, A., Romero-Forte, C., Bolívar, J.P., 2024. Assessment of metal (loid) and natural radionuclide pollution in surface sediments of an estuary affected by mining and phosphogypsum releases. Environ. Sci. Pollut. Res. 31 (39), 51489–51503.

Grande, J.A., De la Torre, M.L., Cerón, J.C., Beltrán, R., Gómez, T., 2010. Overall hydrochemical characterization of the Iberian Pyrite Belt. Main acid mine drainage-generating sources (Huelva, SW Spain). J. Hydrol. 390 (3–4), 123–130.

Grande, J.A., Valente, T., De la Torre, M.L., Santisteban, M., Cerón, J.C., Pérez-Ostalé, E., 2014. Characterization of acid mine drainage sources in the Iberian Pyrite Belt: base methodology for quantifying affected areas and for environmental management. Environ. Earth Sci. 71 (6), 2729–2738.

Gumbo, N., Kapenge, C., 2025. Groundwater Contaminated with Heavy Metals as a Threat to Population Safety and Health in developing Countries: a Scoping Review. Trends in Ecological and Indoor Environmental Engineering 3 (2), 37–45.

Huang, Y.P., 1989. Triangular irregular network generation and topographical modeling. Comput. Ind. 12 (3), 203–213.

Inverno, C., Díez-Montes, A., Rosa, C., García-Crespo, J., Matos, J., García-Lobón, J. L., ... & Sousa, P., 2015. Introduction and geological setting of the Iberian Pyrite Belt. 3D, 4D and predictive modelling of major mineral belts in Europe, 191-208.

Karachaliou, T., Protonotarios, V., Kaliampakos, D., Menegaki, M., 2016. Using risk assessment and management approaches to develop cost-effective and sustainable mine waste management strategies. Recycling 1 (3), 328–342.

Kruzhilko, O., Maystrenko, V., Volodchenkova, N., Vambol, S., Ghoumah, F., 2024. Mathematical Description of Harmful Industrial Factors for Assessing the Quarry Workers’ Occupational Risk. Trends in Ecological and Indoor Environment Engineering 2 (1), 35–40.

Li, D., Ramos, A.O., Bah, A., Li, F., 2024. Valorization of lead-zinc mine tailing waste through geopolymerization: Synthesis, mechanical, and microstructural properties. J. Environ. Manage. 349, 119501.

Lin, C. H., Kong, C., & Lucey, S, 2018. Learning efficient point cloud generation for dense 3d object reconstruction. In proceedings of the AAAI Conference on Artificial Intelligence (Vol. 32, No. 1).

Liu, Z., Zheng, Y., 2011. Effect of Fe (II) on the formation of iron oxide synthesized from pyrite cinders by hydrothermal process. Powder Technol. 209 (1–3), 119–123.

Lowe, D.G., 2004. Distinctive image features from scale-invariant keypoints. Int. J. Comput. Vis. 60, 91–110.

Lucas, J., Lucas, P., Le Mercier, T., Rollat, A., & Davenport, W., 2015. Rare earth production, use and price. Rare Earths: Science, Technology, Production and Use; Elsevier: Amsterdam, The Netherlands, 1-19.

Martín-Velázquez, S., Rodríguez-Santalla, I., Ropero-Szymańska, N., Gomez-Ortiz, D., Martín-Crespo, T., de Ignacio-San José, C., 2022. Geomorphological mapping and erosion of abandoned tailings in the hiendelaencina Mining District (Spain) from Aerial Imagery and LiDAR Data. Remote Sens. (Basel) 14 (18), 4617.

Mouslopoulou, V., Moraetis, D., Fassoulas, C., 2011. Identifying past earthquakes on carbonate faults: advances and limitations of the ‘Rare Earth Element’method based

on analysis of the Spili Fault, Crete. Greece. Earth and Planetary Science Letters 309 (1–2), 45–55.
Mu, Y., Peng, Y., Lauten, R.A., 2016. The depression of pyrite in selective flotation by different reagent systems–a Literature review. Miner. Eng. 96, 143–156.
Navarro-Ramos, S.E., Sparacino, J., Rodríguez, J.M., Filippini, E., Marsal-Castillo, B.E., García-Cannata, L., Torres, R.C., 2022. Active revegetation after mining: what is the contribution of peer-reviewed studies? Heliyon 8 (3).
Nieto, J.M., Sarmiento, A.M., Olías, M., Canovas, C.R., Riba, I., Kalman, J., Delvalls, T.A., 2007. Acid mine drainage pollution in the Tinto and Odiel rivers (Iberian Pyrite Belt, SW Spain) and bioavailability of the transported metals to the Huelva Estuary. Environ. Int. 33 (4), 445–455.
Patil, A.B., Paetzel, V., Struis, R.P., Ludwig, C., 2022. Separation and recycling potential of rare earth elements from energy systems: feed and economic viability review. Separations 9 (3), 56.
Pérez-López, R., Nieto, J.M., de Almodóvar, G.R., 2007. Immobilization of toxic elements in mine residues derived from mining activities in the Iberian Pyrite Belt (SW Spain): laboratory experiments. Appl. Geochem. 22 (9), 1919–1935.
Pinedo Vara, I., 1963. Piritas de Huelva. Summa, Madrid, p. 1003.
Pirti, A., 2011. Evaluating the repeatability of RTK GPS. Surv. Rev. 43 (320), 177–186.
Quindos, L.S., Fernandez, P.L., Soto, J., Rodenas, C., Gomez, J., 1994. Natural radioactivity in spanish soils. Health Phys. 66 (2), 194–200.
Ramírez-Pérez, J.A., Gázquez-González, M.J., Bolívar, J.P., 2025. Valorization Diagnosis of Roasted Pyrite Ashes Wastes from the Iberian Pyrite Belt. Recycling 10 (3), 112.
Sánchez-Donoso, R., Martín-Duque, J.F., Crespo, E., Higueras, P.L., 2019. Tailing's geomorphology of the San Quintín mining site (Spain): landform catalogue, aeolian erosion and environmental implications. Environ. Earth Sci. 78, 1–17.
Santos, Á.M., Teresa, L.C.A., Llácer, J.M.M., Romero, M.I., Manjón, M.D.M.P.P., del Llano, S.L.L., 2022. Real Decreto 1029/2022, de 20 de Diciembre, por el que se Aprueba el Reglamento Sobre Protección de la Salud Contra los Riesgos Derivados de la Exposición a las Radiaciones Ionizantes: Preguntas y Respuestas. Madrid, Spain, Agencia Estatal Boletín Oficial del Estado.
Shabalala, A.N., Ekolu, S.O., Diop, S., 2014. Permeable reactive barriers for acid mine drainage treatment: a review. Construction Materials and Structures 1416–1426.
Szeliski, R., 2022. Computer vision: algorithms and applications. Springer Nature.
Terrones-Saeta, J.M., Suárez-Macías, J., Bernardo-Sánchez, A., Álvarez de Prado, L., Menéndez Fernández, M., Corpas-Iglesias, F.A., 2021. Treatment of soil contaminated by mining activities to prevent contamination by encapsulation in ceramic construction materials. Materials 14 (22), 6740.
Tucci, G., Gebbia, A., Conti, A., Fiorini, L., Lubello, C., 2019. Monitoring and computation of the volumes of stockpiles of bulk material by means of UAV photogrammetric surveying. Remote Sens. (Basel) 11 (12), 1471.
Tunsu, C., Ekberg, C., Retegan, T., 2014. Characterization and leaching of real fluorescent lamp waste for the recovery of rare earth metals and mercury. Hydrometall. 144, 91–98.
Wrixon, A.D., 2008. New ICRP recommendations. J. Radiol. Prot. 28 (2), 161.
Yesares, L., González-Jiménez, J.M., Jiménez-Cantizano, F.A., González-Pérez, I., Caro-Moreno, D., Sánchez, I.M., 2023. Unveiling High-Tech Metals in Roasted Pyrite Wastes from the Iberian Pyrite Belt. SW Spain. Sustainability 15 (15), 12081.
Zietara, A. M., 2017. Creating Digital Elevation Model (DEM) based on ground points extracted from classified aerial images obtained from Unmanned Aerial Vehicle (UAV) (Master's thesis, NTNU).